Research Article Vol. 29, No. 6 / 15 March 2021 / Optics Express 9231
Optics EXPRESS

Comparative study on resolution enhancements in fluorescence-structured illumination Fresnel incoherent correlation holography

PHILJUN JEON,[1] JONGWU KIM,[1] HEEJUNG LEE,[1] HYUK-SANG KWON,[2] AND DUG YOUNG KIM[1,*]

[1]Physics Department, Yonsei University, 50 Yonsei-ro, Seodaemun-gu, Seoul, Republic of Korea
[2]Gwangju Institute of Science and Technology, Department of Biomedical Science and Engineering, 123 Cheomdan-gwagiro, Buk-gu, Gwangju 61005, Republic of Korea
*dykim1@yonsei.ac.kr

Abstract: Fresnel incoherent correlation holography (FINCH) is a new approach for incoherent holography, which also has enhancement in the transverse resolution. Structured illumination microscopy (SIM) is another promising super-resolution technique. SI-FINCH, the combination of SIM and FINCH, has been demonstrated lately for scattering objects. In this study, we extended the application of SI-FINCH toward fluorescent microscopy. We have built a versatile multimodal microscopy system that can obtain images of four different imaging schemes: conventional fluorescence microscopy, FINCH, SIM, and SI-FINCH. Resolution enhancements were demonstrated by comparing the point spread functions (PSFs) of the four different imaging systems by using fluorescence beads of 1-μm diameter.

1. Introduction

Ever since Gabor's first paper, holography has been considered one of the most desirable future imaging and display technology [1]. Interference patterns are required in holography, and a laser source with a long coherence length is typically used. Even though holography with a broadband light source (e.g., a light bulb, an LED, or a fluorescence molecule) is highly desired in many practical applications, a broadband light source is hardly utilized in holographic imaging due to its short coherence length. Various approaches have been reported lately to adapt natural light sources in holography: rotational shearing interferometer [2–4], triangle interferometer [5–7], conoscopic holography [8–10], scanning holography [11,12], Fourier incoherent single-channel holography (FISCH) [13,14], Fresnel incoherent correlation holography (FINCH) [15–17], self-interference digital holography (SIDH) [18,19], coded aperture correlation holography (COACH) [20], diffuser CAM [21,22], and chaotic waves imaging [23]. FINCH is one of the most successful approaches to incoherent holography, where the common-path self-interference system uses a spatial light modulator (SLM). J. Rosen [24,25] also showed that the transverse resolution of FINCH can be twice the resolution of a conventional coherent imaging system.

Structured illumination microscopy (SIM) is a super-resolution imaging scheme that uses structured illumination patterns on a target sample [26–29]. SIM can be adapted to many conventional imaging systems simply by changing the illumination part of an imaging system while keeping the other parts unchanged. Various combinations of SIM and other optical imaging systems have been demonstrated lately, e.g. digital holographic microscopy (DHM) [30], Total internal reflection fluorescent microscopy (TIRF) [31], photoacoustic system [32], and FINCH [33]. SI-FINCH is a combination of SIM and FINCH. Since SIM and FINCH improve the transverse resolution of an imaging system independently with different principles, a combined system is expected to have unprecedented performance. Y. Kashter et al. reported resolution improvements by using SI-FINCH for a scattering object, a USAF resolution target, with a LED

#417206 https://doi.org/10.1364/OE.417206
Journal © 2021 Received 10 Dec 2020; revised 19 Feb 2021; accepted 23 Feb 2021; published 10 Mar 2021

Optics EXPRESS

source [33]. In their work, SI-FINCH was demonstrated with scattering objects, and two SLMs were used: one for SI pattern generation and another one for FINCH.

In this paper, we used a DMD for SI pattern generation, which is a cost-effective device. We have demonstrated the possibility of extending the usage of SI-FINCH toward fluorescent microscopy, the greatest application area of super-resolution imaging. By imaging multiple fluorescent beads on a plane, we compared the resolutions of conventional fluorescent imaging, FINCH, SIM, and SI-FINCH. We believe our work paves the road toward wide-field super-resolution fluorescence SI-FINCH for biomedical imaging. This paper is organized as follows. Section 2 explains the principles of the transverse resolution improvement in FINCH and SI systems. Section 3 presents the experiment system. Section 4 shows measurement results and improvements in point spread function (PSF) and visibility using SI-FINCH. Finally, section 5 discusses improvements and possible applications of SI-FINCH toward super-resolution fluorescence microscopy.

2. Principles

2.1. Transverse resolution enhancement in FINCH

In conventional holography, interference patterns between a reference light and an object light are obtained by making the coherence length of a light source larger than the optical path length difference (OPD) of two lights. Although the coherence length of incoherent light is increased by reducing its spectral width with a band-pass filter, it is hard to obtain an interference pattern with the separated reference wave. Self-interference obtains a hologram with only object wave that it interferes, itself, with very short OPD. FINCH embodies self-interference as a common-path interferometer with SLM; common-path configuration suppresses OPD and can occur interference with the short coherent length. The object wave is modulated with two different phase patterns when it passes through an SLM, and they superimpose on the detector to form an interference pattern. An SLM modulates light with a specific polarization direction, while the other orthogonally polarization light is not modulated by SLM; for interference phenomenon, polarizer should make the polarization of both wave in axis with 45° angles linear polarizer. Figure 1 shows the beam paths in a typical FINCH setup built with an SLM.

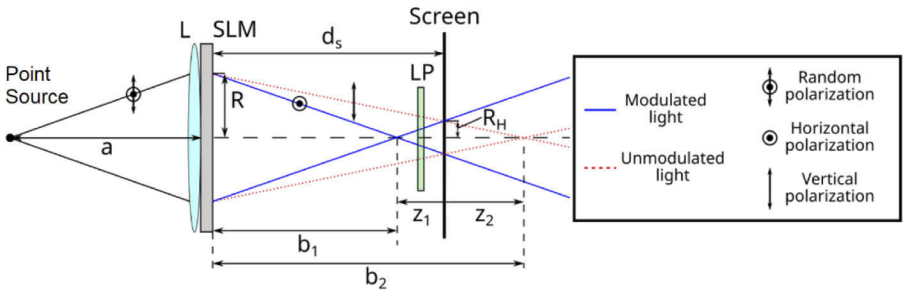

Fig. 1. Schematic diagram to show the principles of our FINCH system. L is a positive lens to make unmodulated light (vertically polarized component) focused on a plane located at b_2 distance from an SLM. The SLM modulates only the horizontal polarization component of randomly polarized fluorescence light emitted from a point source. LP is a linear polarizer whose transmission angle is 45 degrees from the vertical direction. b_1 is distance from the SLM to the focusing point of the horizontally polarized light.

Because FINCH is a hybrid imaging system, it has modified Lagrange invariants; unlike a conventional system, the magnification of PSF does not match the transverse magnification in FINCH [24,25]. The following derivations are to show the mismatch between transverse magnification and the PSF magnification in FINCH. Since the SLM shown in Fig. 1 only modulates the phase of horizontally polarized light, it produces two different wavefronts. The

Optics EXPRESS

distance from the SLM to the focusing point of the horizontally polarized light is b_1, while that of the vertically polarized light is b_2. The distance from the SLM to the screen is d_s. The horizontally polarized light is diverging on the screen and has a radius of curvature z_1. The vertically polarized light is converging on the screen and has a radius of curvature is z_2. A hologram is formed on the screen by these two different wavefronts. The measured hologram has a radius of curvature z_c given with the following equation [34].

$$z_c = \left|\frac{z_1 z_2}{z_2 - z_1}\right| = \left|\frac{(d_s - b_1)(d_s - b_2)}{b_2 - b_1}\right| \tag{1}$$

In Fig. 1 we define R as the radius of pupil aperture, which is the radius of the SLM. We define R_{H1} and R_{H2} as the size or the maximum radii of the two beams on the screen. If we define R_H as the radius of the interference pattern on the screen, R_H is the smaller of R_{H1} and R_{H2}. We have $R_{H1}<R_{H2}$ when $d_s<\frac{2b_1b_2}{b_1+b_2}$, and $R_{H1}>R_{H2}$ when $d_s>\frac{2b_1b_2}{b_1+b_2}$. In Fig. 1 the screen is placed where the sizes of the two beams are equal: $d_s = \frac{2b_1b_2}{b_1+b_2}$ and $R_{H1} = R_{H2}$. The size of a hologram R_H is related to the size of the SLM R with the proportionality factor α.

$$R_H = \alpha R \quad where\ \alpha = \begin{cases} \frac{d_s - b_1}{b_1} & when\ \ d_s < \frac{2b_1b_2}{b_1+b_2} \\ \frac{d_s - b_2}{b_2} & when\ \ d_s > = \frac{2b_1b_2}{b_1+b_2} \end{cases} \tag{2}$$

We define the full width at half-maximum of the PSF as the spot size W_i in the image plane. Then, we have $W_i \approx 0.61\lambda/NA_i$, where NA_i is the numerical aperture of a converging wavefront in the image plane. If we use the paraxial approximation, the NAs of the two wavefronts in the image plane become $NA_{1i} \approx R/b_1$ and $NA_{2i} \approx R/b_2$. These two NAs produce two different spot sizes: $W_{ni} = 0.61\lambda/NA_n \approx 0.61\lambda b_n/R : n = 1, 2$. We can convert the spot sizes of the two beams in the image space $W_{ni} : n = 1, 2$ into the spot sizes of two corresponding beams in the object space $W_{no} : n = 1, 2$. The transverse magnifications of the two spots are b_1/a and b_2/a, we obtain the same spot size for the two beams in the object space: $W_{no} = 0.61\lambda a/R : n = 1, 2$. The NA of the hologram in the image plane becomes $NA_{Hi} \approx R_H/Z_c$ with the paraxial approximation. Then, the spot size produced by the hologram can be written as Eq. (3).

$$W_{Hi} = \frac{0.61\lambda}{NA_{Hi}} = \frac{0.61\lambda z_c}{R_H} = \begin{cases} \frac{0.61\lambda z_c}{R} \cdot \frac{b_1}{d_s - b_1} & when \quad d_s > = \frac{2b_1b_2}{b_1+b_2} \\ \frac{0.61\lambda z_c}{R} \cdot \frac{b_2}{d_s - b_2} & when \quad d_s > = \frac{2b_1b_2}{b_1+b_2} \end{cases} \tag{3}$$

We can convert the spot sizes of the hologram in the image space W_{Hi} into the spot sizes of two corresponding beams in the object space W_{Ho}. In this case, the transverse magnification of the spot generated by the hologram becomes $(b_s + z_c)/a \approx b_s/a$. Then, we obtain

$$\begin{aligned} W_{no} &= W_{ni} \cdot \tfrac{a}{b_n} = \tfrac{0.61\lambda a}{R} \\ W_{Ho} &= W_{Hi} \cdot \tfrac{a}{d_s} = \tfrac{0.61\lambda a}{R} \cdot \left|\tfrac{(d_s - b_1)(d_s - b_2)}{\alpha(b_2 - b_1)d_s}\right| = \tfrac{0.61\lambda a}{R}\beta \end{aligned} \tag{4}$$

Equation (4) shows that the transverse resolution of FINCH is determined by the NA of the wavefront retrieved from a hologram, which changes depending on the position of the hologram plane relative to the two interfering beams. The smallest value of β is 0.5 when $d_s = \frac{2b_1b_2}{b_1+b_2}$ and $R_{H1} = R_{H2}$. When $\beta = 0.5$ FINCH's transverse two-point resolution is twice better than the conventional coherent imaging system. This is when the two beams overlap perfectly on the screen in Fig. 1.

Because FINCH is in-line holography, the phase-shifting method is necessary to extract phase information from the hologram [35]. The Phase-shiting method requires three phase-shifted

Optics EXPRESS

holograms. In FINCH, SLM shifts the phase of the modulated light with electrical control. FINCH hologram with phase-shifting is given by Eq. (5) where the value of the shifted phase is θ_i.

$$\begin{aligned} h_i &= |E_1(\phi_1) + E_2^i(\phi_2, \theta_i)|^2 = E_1^* E_2^i + C.C. + Const. \\ &= A_1 A_2 e^{-i(\phi_1+\theta_i)} e^{-i\phi_2} + C.C. + Const. \\ where\ \theta_i &= \begin{cases} 0 & when\ \ i = 1 \\ 2\pi/3 & when\ \ i = 2 \\ 4\pi/3 & when\ \ i = 3 \end{cases} \end{aligned} \tag{5}$$

ϕ_1 and ϕ_2 indicates the phase information of each wave. Three phase-shifted holograms are utilized to extract the complex object field H on the hologram plane by using the following equation.

$$\begin{aligned} H &= h_1(e^{i\theta_3} - e^{-i\theta_2}) + h_2(e^{i\theta_1} - e^{-i\theta_3}) + h_3(e^{i\theta_2} - e^{-i\theta_1}) \\ &= A_H e^{i(\phi_1 - \phi_2)} = A_H e^{i\phi_c} \end{aligned} \tag{6}$$

ϕ_c is the phase of complex object field H. In the end, the object field H is back-propagated from the hologram plane to an image plane using the Fresnel back-propagation algorithm [36]. A focused image is obtained by adjusting the backpropagation distance such that the focusing parameter is maximized. We used the Sobel variance as the focusing parameter [37,38].

2.2. Structured illumination microscopy

Structured illumination microscopy (SIM) [29] extracts the high spatial frequency information of a sample beyond the cut-off frequency of a conventional imaging system. The conventional system can obtain the frequency information of an object up to the cut-off frequency illustrated with a thin solid line in Fig. 2(a). In SIM, the high spatial frequency information is shifted toward the measurable frequency range within the cut-off frequency by using a specific illumination pattern. The intensity pattern of illumination light can be written with Eq. (7). It is a sinusoidal intensity pattern with a period along the r-direction with a constant spatial frequency k_1. m is a parameter describing the visibility of the sinusoidal intensity pattern. Figure 2(b) shows the position of the spatial frequency k_1 in the frequency-domain. Here, k_1 is chosen to be the same as the cut-off frequency of an optical imaging system. The accent symbol ~ expresses the Fourier transformed function of the original function.

$$\begin{aligned} I(r; k_1) &= I_O[1 + m \times cos(2\pi k_1 r + \varphi)] \\ \widetilde{I}(k; k_1) &= I_O\left[\delta(k) + \tfrac{m}{2}\{e^{i\varphi}\delta(k - k_1) + e^{i\varphi}\delta(k + k_1)\}\right] \end{aligned} \tag{7}$$

The image intensity S by the structured light is the product of the object intensity O and the structured illumination intensity I. In the frequency domain, this product relation becomes the convolution relation, written as Eq. (8). The operator $\otimes$ indicates the convolution relation in Eq. (8).

$$\begin{aligned} S(r; k_1) &= [I(r) \times O(r)] \otimes PSF(r) \\ \widetilde{S} &= [\widetilde{I}(k; k_1) \otimes \widetilde{O}(k)] \cdot OTF(k) \\ &= I_O\left[\widetilde{O}(k) + \tfrac{m}{2} e^{i\varphi}\{\widetilde{O}(k - k_1) + \widetilde{O}(k + k_1)\}\right] \cdot OTF(k) \end{aligned} \tag{8}$$

Figure 2 shows the basic principle and procedures used in SI-FINCH. The OTF of FINCH is illustrated as a solid circle in Fig. 2(a), while red dotted circles in Figs. 2(a) and 2(c) filled with gradient blue represent object function $\tilde{O}(k)$ used in Eq. (8). We consider a case where the

Optics EXPRESS

maximum frequency of an object function Õ(k) is larger than the cutoff frequency of a FINCH system. Figure 2(c) illustrates the three overlapped frequency components within the measurable range of an optical system. In order to extract the original frequency function of an object from the three overlapped functions, three different measurements are necessary. $\widetilde{S}$ are necessary with different φ for three independent linear equations because $\widetilde{S}$ is the superposition of three $\widetilde{O}$ with frequency shifting. After computation, the frequency spectrum is expanded by adding a high frequency of $\widetilde{O}(k \pm k_O)$ on $\widetilde{O}(k)$, as shown in Fig. 2(d). To obtain all high-frequency components within the two-dimensional space, at least three sets of measurements with different directions of the spatial frequency are needed. Figure 2(e) shows the three different shifted pattern images obtained for three different directions; total nine images are needed for a single SIM image. We used OpenSIM, the open-source SIM reconstruction algorithm [28] with eight axes structured illumination patterns.

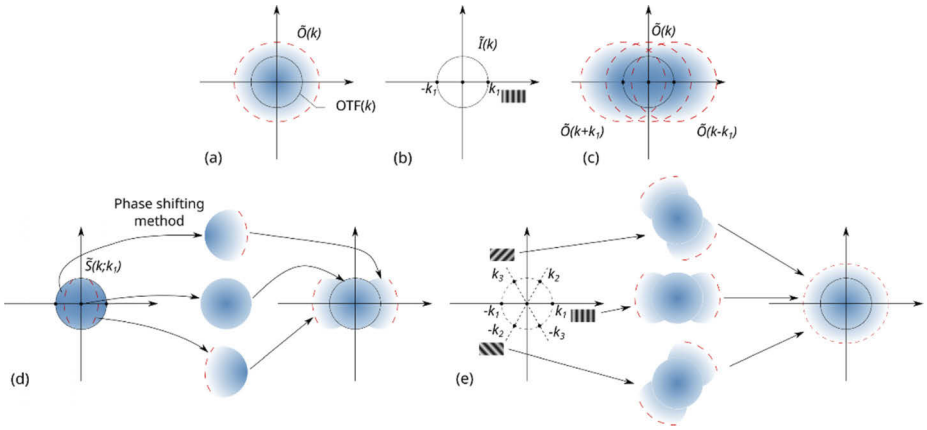

Fig. 2. The principle of SIM explained in the frequency domain. (a) Object information in the frequency domain $\tilde{O}$, (b) Horizontal SI pattern in frequency domain $\tilde{I}$, (c) SI image in frequency domain for horizontal SI in (b), (d) Extracting and adding high spatial frequency information by the phase-shifting method and (e) Three axes SI imaging for isotropic expansion.

3. Experimental setup

Our proposed SI-FINCH system is shown in Fig. 3. It consists of a structured pattern generator combined with a FINCH system. A green DPSS laser at 532 nm wavelength is used as an excitation light source. There are several schemes to generate a sinusoidal structured pattern on a sample, e.g. grating [27], SLM [39,40], and DMD [41,42]. We used a DMD (DLP Lightcrafter 6500) in our SIM setup. It can generate sinusoidal patterns on a sample with a pattern pitch size ranging from 1.6 ~ 1.9 um. A DC filter is placed on the Fourier plane of a 4f-system shown in Fig. 3 to remove unwanted peaks in structured light patterns made by the DMD. A 4f-system is made with two achromatic lenses of 15 cm focal length. We used red fluorescence beads of 1-μm diameter (580/605 ThermoFisher FluoSpheres) as a sample. The size of a bead is smaller than the resolution of our imaging system since we used an objective lens of NA = 0.25 (Olympus x10, 0.25NA). The diffraction-limited resolution of the imaging system becomes $0.605\mu m/(2 \cdot 0.25) = 1.21\mu m$. Each fluorescence bead can be considered as a point source because we used a low-NA objective lens whose transverse resolution is much larger than the diameter of the beads.

We build a FINCH system by using an SLM (Holoeye PLUTO VIS-056, 8um pixel pitch). An objective lens and a tube lens are put in front of the SLM. The orientation of the SLM in Fig. 1 is

Optics EXPRESS

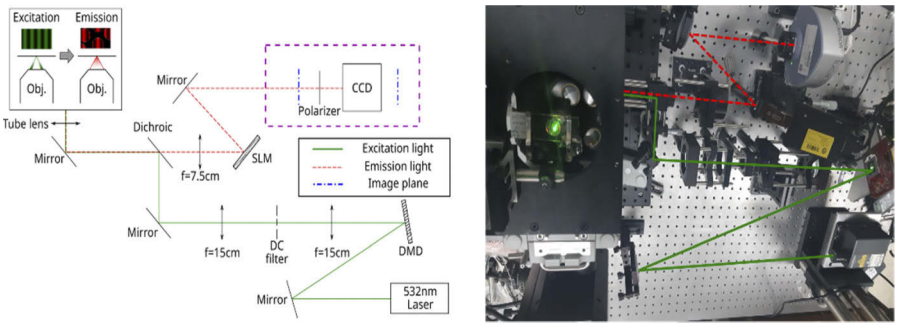

Fig. 3. Schematic diagram of our SI-FINCH setup (left) and its picture (right). Detailed ray tracings for two interfering beams near a CCD are shown in Fig. 4 (a).

arranged such that the wavefront of horizontally polarized light through the SLM is modulated. The wavefront of vertically polarized light, which is illustrated with red dotted lines in Fig. 1, is not modified by the SLM.

We applied three phase-shifted modulation masks shown in Figs. 4(b)–4(d) to the SLM and acquired three phase-shifted holograms. Examples of raw holograms are shown in Fig. 5(a). Figure 5(b) shows the phase and the amplitude of a complex optical field calculated from the three phase-shifted holograms. Two blue dot-dashed lines on both sides of a CCD in Fig. 3 represent the two focusing planes of the two wavefronts; these are also shown in the ray tracings of Fig. 4(a). b_1 and b_2 in Fig. 1 are the distances from the SLM to these two focusing planes. The axial position of a CCD is adjusted to maximize the overlap area of the two wavefronts on the CCD. As illustrated in Fig. 5, we have acquired 72 (3×3x8) images to make one SI-FINCH image: 3 phase-shifted images for FINCH, 24 structured illumination images for SIM (8-axis SIM and 3 patterned-illumination images for each axis). This system can be switched between FINCH, SIM, SI-FINCH, and conventional image systems by turning the SLM and the DC filter on and off in the setup. We compared the image qualities of the four aforementioned imaging systems.

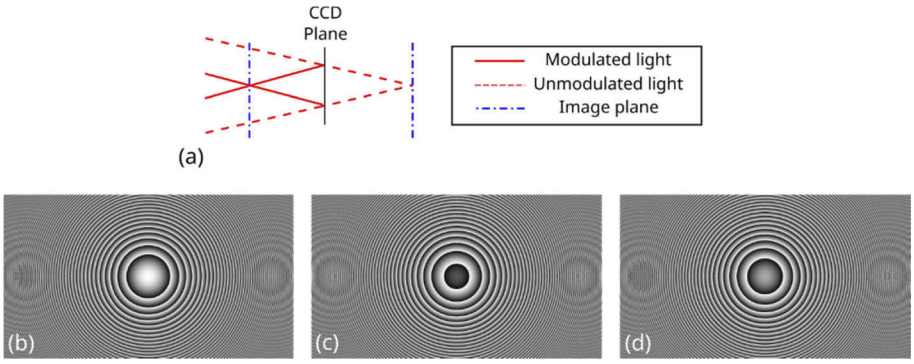

Fig. 4. (a) Ray tracing of two interfering beams on a CCD plane. (b)~(d) Three phase-maps applied to an SLM for phase-shifting in-line holography. The amount of phase delay for light passing through the SLM is proportional to the brightness of a phase map; black represents 0 phase delay, and white corresponds to 2π phase delay. The SLM works as a Fresnel lens of 112 cm focal length for all three cases. The phase delays (θ) at the centers of these phase maps are 2π for (b), $2\pi/3$ for (c), and $4\pi/3$ for (d).

Optics EXPRESS

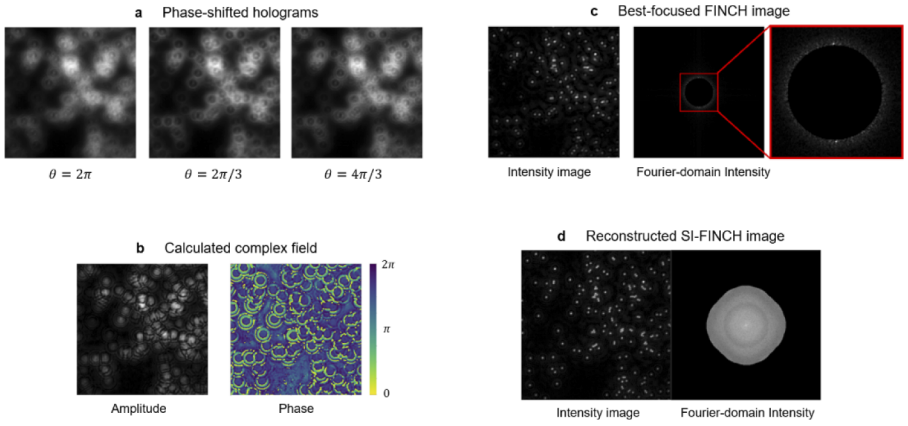

Fig. 5. Data acquisition and image processing sequence of SI-FINCH. (a) Three phase-shifted holograms obtained by using an SLM whose phase-maps are given in Figs. 4(b)–4(d). (b) The amplitude and the phase of the complex optical field calculated from the three phase-shifted holograms shown in Fig. 5(a). (c) An intensity image on its best-focused plane, which is calculated from a complex optical field shown in Fig. 5(b) by using a numerical beam propagation method. (d) SI-FINCH image calculated from 24 best-focused FINCH images, one of which is shown in Fig. 5(c).

4. Result

Figure 6 shows the images of the four imaging systems: (a) conventional microscopy, (b) FINCH, (c) SIM, (d) SI-FINCH. Figures 6(e)-6(h) show the expanded view of a single bead depicted with red squares within images of Figs. 6(a)–6(d). Figures 6(i)–6(l) show the expanded view of four clustered beads depicted with green squares within images of Figs. 6(a)–6(d). The diameter of each red fluorescence bead is 1μm, which is smaller than the conventional imaging system's diffraction-limited resolution of 1.21um. Each figure of Figs. 6(e)–6(h) shows the PSF of each imaging system. Figure 6(e) is the PSF of conventional microscopy, and it shows the largest intensity pattern. Figure 6(h) is the PSF for the SI-FINCH, and it shows the smallest intensity pattern. Figure 6(i) is the image of four lumped beads captured with SI-FINCH, and it clearly shows four beads and their boundaries.

The left figure of Fig. 7 shows Line scan intensity profiles for the four PSF images shown in Figs. 6(e)–6(h). Each profile is normalized by its peak intensity. The left figure of Fig. 7 shows the Gaussian curve fittings for the measured data shown in the left figure of Fig. 7. Because the bead size is smaller than the transverse resolution limit, a single bead image can be considered as its PSF. The full width at half maximum (FWHM) of the Gaussian curve fitting results shown in the right figure of Fig. 7 is listed in Table 1. The FWHM of conventional microscopy is the largest. The FWHM of FINCH is the second largest but is much smaller than that of conventional microscopy. The FWHM of SIM is smaller than that of FINCH. The FWHM of the SI-FINCH is the smallest and has much much improvement compared to that of SIM. The FWHMs of SI-FINCH, SIM, and FINCH are reduced by 36.68%, 20.08%, and 14.85% compared to the FWHM of conventional microscopy, respectively. When SI-FINCH is compared with the SIM, the FWHM of SI-FINCH is about 23.18% narrower than that of SIM. It means the transverse resolution improvement of both techniques is synergically enhanced with each other.

Figure 8 shows the line scan normalized intensity profiles across the red lines on the images captured by the four different imaging schemes: conventional microscopy, FINCH, SIM, and SI-FINCH. Even though the object is made of four clustered beads, images obtained by FINCH and conventional microscopy cannot distinguish individual beads within the cluster. Four beads

Optics EXPRESS

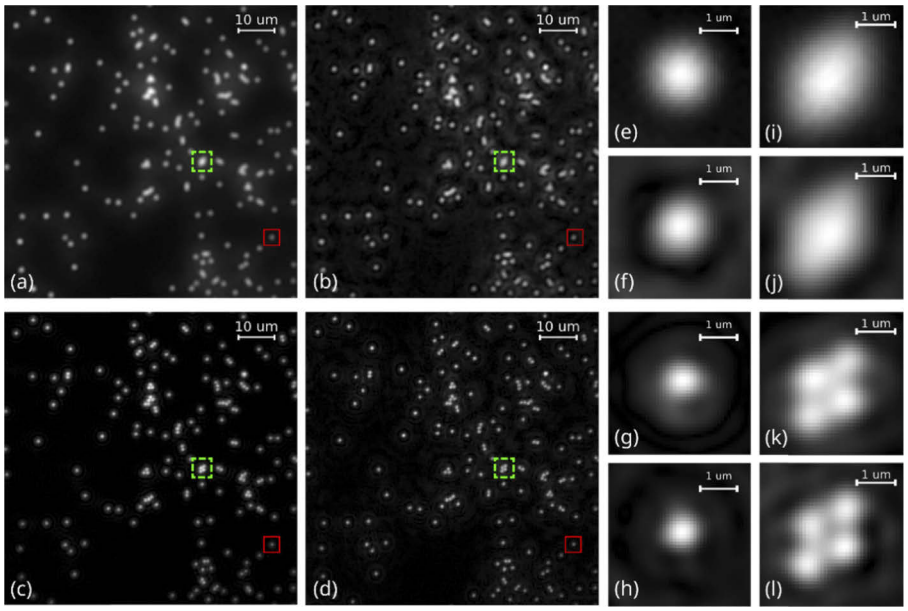

Fig. 6. (a-d) Measured images of fluorescence beads of 1μm diameter on a microscope slide by different imaging schemes. (e-h) Magnified images of a single bead within the red squares in Fig. 6(a-d). (i-l) Magnified images of four clustered beads within the green dashed squares in Fig. 6(a-d). (a), (e), (i): Conventional microscopy (b), (f), (j): FINCH (c), (g), (k): SIM (d), (h), (l): SI-FINCH

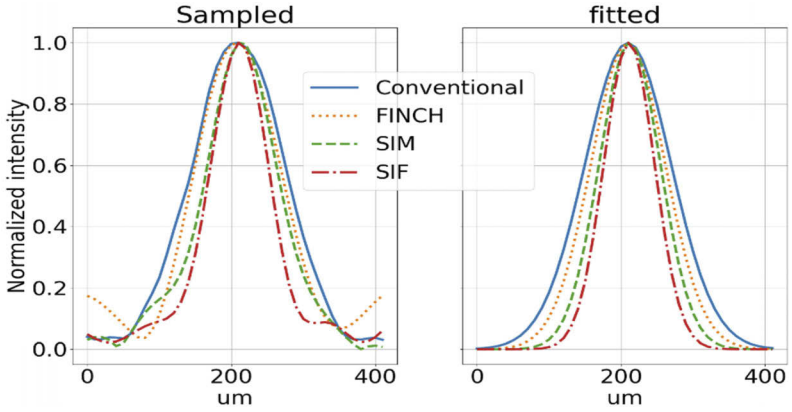

Fig. 7. Line scan intensity profiles of a single isolated bead from the PSF images shown in Figs. 4(e)–4(h) and their Gaussian curve fittings.

Table 1. FWHM of the Gaussian fitted curve for each imaging method (μm)

System	Conventional	FINCH	SIM	SI-FINCH
FWHM	72.80	61.99	58.18	44.69

Optics EXPRESS

look like a big single object with conventional microscopy and FINCH. The line profile from the SIM image shows a shallow dip at the center. The line scan image by SI-FINCH shows a clear dip at the center.

$$Visibility = \frac{I_{peak} - I_{bottom}}{I_{peak} + I_{bottom}} \quad where \quad I_{peak} = \frac{I_{peak1} + I_{peak2}}{2} \tag{9}$$

The visibilities of two adjacent peaks are calculated by using Eq. (9). We used the mean of two peak values as I_{peak}. We obtained the visibility of SI-FINCH shown in Fig. 8(g) is 0.17, while that of SIM for Fig. 8(h) is 0.09. Compared to SIM, SI-FINCH shows an almost two-fold improvement in visibility.

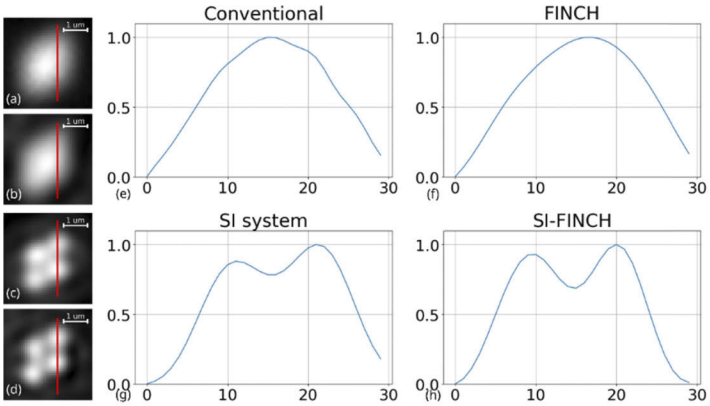

Fig. 8. Magnified images of four clustered beads captured by (a) conventional microscopy, (b) FINCH, (c) SIM, and (d) SI-FINCH. Line scan normalized intensity profiles across the red lines on the expanded images.

5. Conclusions

FINCH is a new powerful holographic imaging technique that has much improved transverse resolution compared to conventional microscopy. And lately, SI-FINCH, a combination of SIM and FINCH was demonstrated to enhance the transverse resolution even further. In a case where one of the enhanced resolution techniques e.g., synthetic aperture, structured illumination, coded aperture mask combined with FINCH, unlike equivalent incoherent imaging system, the uniform frequency response or flat cylindrical ATF of FINCH provides the ability to increase the frequency response of the higher frequencies located at the peripheral areas. Therefore, SI-FINCH is better than equivalent SIM with a conventional imaging scheme in terms of lateral resolution.

In this paper, have extended the application of SI-FINCH toward fluorescence microscopy applications. By using an SLM and a DMD, we have built a versatile multimodal microscopy system that can obtain four different widefield fluorescence images of a sample: conventional microscopy, FINCH, SIM, and SI-FINCH. We have measured and compared the resolutions of these four imaging modalities by measuring their PSFs. The PSF of each imaging scheme was directly obtained by measuring fluorescence beads of 1-μm diameter on a microscope slide. Fluorescence beads produce strong fluorescence signals, while each of them can be considered as a point source because we used a low-NA objective lens whose transverse resolution is 1.21 μm, which is much larger than the diameter of the beads. Our results show that the FWHMs of SI-FINCH, SIM, and FINCH are reduced by 36.68%, 20.08%, and 14.85%, respectively, compared to that of conventional microscopy. SIM has a side-effect of generating sidelobes as

Optics EXPRESS

shown in Fig. 6, and there are several related reports on effective methods to reduce sidelobes in SIM images [43].

Funding. National Research Foundation of Korea (2017R1A2B4003950); Korea Institute for Advancement of Technology (P0011925).

Disclosures. The authors declare that there are no conflicts of interest related to this article.

References

1. D. Gabor, "A New Microscopic Principle," Nature **161**(4098), 777–778 (1948).
2. M. V. R. K. Murty and E. C. Hagerott, "Rotational–Shearing Interferometry," Appl. Opt. **5**(4), 615–619 (1966).
3. T. Nomura, K. Itoh, and Y. Ichioka, "Hybrid high speed pattern matching using a binary incoherent hologram generated by a rotational shearing interferometer," Appl. Opt. **28**(23), 4987–4991 (1989).
4. K. Watanabe and T. Nomura, "Recording spatially incoherent Fourier hologram using dual channel rotational shearing interferometer," Appl. Opt. **54**(1), A18–A22 (2015).
5. G. Cochran, "New Method of Making Fresnel Transforms with Incoherent Light*," J. Opt. Soc. Am. **56**(11), 1513–1517 (1966).
6. S.-G. Kim, B. Lee, and E.-S. Kim, "Removal of bias and the conjugate image in incoherent on-axis triangular holography and real-time reconstruction of the complex hologram," Appl. Opt. **36**(20), 4784–4791 (1997).
7. Y. Wan, T. Man, and D. Wang, "Incoherent off-axis Fourier triangular color holography," Opt. Express **22**(7), 8565–8573 (2014).
8. G. Sirat and D. Psaltis, "Conoscopic holography," Opt. Lett. **10**(1), 4–6 (1985).
9. L. M. Mugnier, G. Y. Sirat, and D. Charlot, "Conoscopic holography: two-dimensional numerical reconstructions," Opt. Lett. **18**(1), 66–68 (1993).
10. L. M. Mugnier, "Conoscopic holography: toward three-dimensional reconstructions of opaque objects," Appl. Opt. **34**(8), 1363–1371 (1995).
11. T.-C. Poon, K. B. Doh, B. W. Schilling, M. H. Wu, K. K. Shinoda, and Y. Suzuki, "Three-dimensional microscopy by optical scanning holography," Opt. Eng. **34**(5), 1338–1344 (1995).
12. G. Indebetouw and W. Zhong, "Scanning holographic microscopy of three-dimensional fluorescent specimens," J. Opt. Soc. Am. A **23**(7), 1699–1707 (2006).
13. R. Kelner and J. Rosen, "Spatially incoherent single channel digital Fourier holography," Opt. Lett. **37**(17), 3723–3725 (2012).
14. R. Kelner, J. Rosen, and G. Brooker, "Enhanced resolution in Fourier incoherent single channel holography (FISCH) with reduced optical path difference," Opt. Express **21**(17), 20131–20144 (2013).
15. J. Rosen and G. Brooker, "Digital spatially incoherent Fresnel holography," Opt. Lett. **32**(8), 912–914 (2007).
16. J. Rosen and G. Brooker, "Non-scanning motionless fluorescence three-dimensional holographic microscopy," Nat. Photonics **2**(3), 190–195 (2008).
17. N. Siegel, V. Lupashin, B. Storrie, and G. Brooker, "High-magnification super-resolution FINCH microscopy using birefringent crystal lens interferometers," Nat. Photonics **10**(12), 802–808 (2016).
18. J. Hong and M. K. Kim, "Single-shot self-interference incoherent digital holography using off-axis configuration," Opt. Lett. **38**(23), 5196–5199 (2013).
19. C. Jang, D. C. Clark, J. Kim, B. Lee, and M. K. Kim, "Signal enhanced holographic fluorescence microscopy with guide-star reconstruction," Biomed. Opt. Express **7**(4), 1271–1283 (2016).
20. A. Vijayakumar, Y. Kashter, R. Kelner, and J. Rosen, "Coded aperture correlation holography–a new type of incoherent digital holograms," Opt. Express **24**(11), 12430–12441 (2016).
21. N. Antipa, G. Kuo, R. Heckel, B. Mildenhall, E. Bostan, R. Ng, and L. Waller, "DiffuserCam: lensless single-exposure 3D imaging," Optica **5**(1), 1–9 (2018).
22. G. Kuo, N. Antipa, R. Ng, and L. Waller, "3D Fluorescence Microscopy with DiffuserCam," in *Imaging and Applied Optics 2018 (3D, AO, AIO, COSI, DH, IS, LACSEA, LS&C, MATH, PcAOP) (2018)* (Optical Society of America, 2018), p. CM3E.3.
23. V. Anand, S. H. Ng, J. Maksimovic, D. Linklater, T. Katkus, E. P. Ivanova, and S. Juodkazis, "Single shot multispectral multidimensional imaging using chaotic waves," Sci. Rep. **10**(1), 13902 (2020).
24. J. Rosen, N. Siegel, and G. Brooker, "Theoretical and experimental demonstration of resolution beyond the Rayleigh limit by FINCH fluorescence microscopic imaging," Opt. Express **19**(27), 26249–26268 (2011).
25. J. Rosen and R. Kelner, "Modified Lagrange invariants and their role in determining transverse and axial imaging resolutions of self-interference incoherent holographic systems," Opt. Express **22**(23), 29048–29066 (2014).
26. M. G. L. Gustafsson, "Surpassing the lateral resolution limit by a factor of two using structured illumination microscopy," J. Microsc. **198**(2), 82–87 (2000).
27. R. Heintzmann and C. G. Cremer, "Laterally modulated excitation microscopy: improvement of resolution by using a diffraction grating," in Optical Biopsies and Microscopic Techniques III (International Society for Optics and Photonics, 1999), Vol. 3568, pp. 185–196.
28. A. Lal, C. Shan, and P. Xi, "Structured Illumination Microscopy Image Reconstruction Algorithm," IEEE J. Sel. Top. Quantum Electron. **22**(4), 50–63 (2016).
29. P. Xi, Optical Nanoscopy and Novel Microscopy Techniques, 1st ed. (CRC Press, 2015).

Optics EXPRESS

30. P. Gao, G. Pedrini, and W. Osten, "Structured illumination for resolution enhancement and autofocusing in digital holographic microscopy," Opt. Lett. **38**(8), 1328–1330 (2013).
31. R. Fiolka, M. Beck, and A. Stemmer, "Structured illumination in total internal reflection fluorescence microscopy using a spatial light modulator," Opt. Lett. **33**(14), 1629–1631 (2008).
32. T. Ilovitsh, A. Ilovitsh, J. Foiret, B. Z. Fite, and K. W. Ferrara, "Acoustical structured illumination for super-resolution ultrasound imaging," Commun. Biol. **1**(1), 3–11 (2018).
33. Y. Kashter, A. Vijayakumar, Y. Miyamoto, and J. Rosen, "Enhanced super resolution using Fresnel incoherent correlation holography with structured illumination," Opt. Lett. **41**(7), 1558–1561 (2016).
34. P. Jeon, H. Lee, J. Kim, C. Liu, and D. Kim, "Analysis of three-dimensional mapping problems in incoherent digital holography," Opt. Express **28**(4), 4501–4515 (2020).
35. I. Yamaguchi and T. Zhang, "Phase-shifting digital holography," Opt. Lett. **22**(16), 1268–1270 (1997).
36. M. K. Kim, "Basic Methods of Numerical Diffraction," in Digital Holographic Microscopy: Principles, Techniques, and Applications 162 (Springer New York, 2011), pp. 43–54.
37. P. Langehanenberg, rn. Kemper Bjö, D. Dirksen, and G. von Bally, "Autofocusing in digital holographic phase contrast microscopy on pure phase objects for live cell imaging," Appl. Opt. **47**(19), D176–D182 (2008).
38. Y. Zhang, H. Wang, Y. Wu, M. Tamamitsu, and A. Ozcan, "Edge sparsity criterion for robust holographic autofocusing," Opt. Lett. **42**(19), 3824–3827 (2017).
39. B.-J. Chang, L.-J. Chou, Y.-C. Chang, and S.-Y. Chiang, "Isotropic image in structured illumination microscopy patterned with a spatial light modulator," Opt. Express **17**(17), 14710–14721 (2009).
40. K. O'Holleran and M. Shaw, "Optimized approaches for optical sectioning and resolution enhancement in 2D structured illumination microscopy," Biomed. Opt. Express **5**(8), 2580–2590 (2014).
41. A. Sandmeyer, M. Lachetta, H. Sandmeyer, W. Hübner, T. Huser, and M. Müller, "DMD-based super-resolution structured illumination microscopy visualizes live cell dynamics at high speed and low cost," *bioRxiv* 797670 (2019).
42. P. T. Brown, R. Kruithoff, G. J. Seedorf, and D. P. Shepherd, "Multicolor structured illumination microscopy and quantitative control of polychromatic coherent light with a digital micromirror device," *bioRxiv* 2020.07.27.223941 (2020).
43. G. Wen, S. Li, L. Wang, X. Chen, Z. Sun, Y. Liang, X. Jin, Y. Tang, and H. Li, "HiFi-SIM: reconstructing high-fidelity structured illumination microscope images," *bioRxiv* 2020.07.16.204875 (2020).